ACS NANO

www.acsnano.org

ARTICLE

Gold Single Atom Doped Defective Nanoporous Copper Octahedrons for Electrocatalytic Reduction of Carbon Dioxide to Ethylene

Yang Zhao,[‖] Yanan Wang,[‖] Zhipeng Yu, Chao Song, Jingwei Wang, Haoliang Huang, Lijian Meng, Miao Liu,* and Lifeng Liu*

Cite This: *ACS Nano* 2025, 19, 4505−4514

Read Online

ACCESS | Metrics & More | Article Recommendations | Supporting Information

ABSTRACT: Electrocatalytic CO_2 reduction into high-value multicarbon products offers a sustainable approach to closing the anthropogenic carbon cycle and contributing to carbon neutrality, particularly when renewable electricity is used to power the reaction. However, the lack of efficient and durable electrocatalysts with high selectivity for multicarbons severely hinders the practical application of this promising technology. Herein, a nanoporous defective Au_1Cu single-atom alloy (De-Au_1Cu SAA) catalyst is developed through facile low-temperature thermal reduction in hydrogen and a subsequent dealloying process, which shows high selectivity toward ethylene (C_2H_4), with a Faradaic efficiency of 52% at the current density of 252 mA cm^{-2} under a potential of −1.1 V versus reversible hydrogen electrode (RHE). In situ spectroscopy measurements and density functional theory (DFT) calculations reveal that the high C_2H_4 product selectivity results from the synergistic effect between Au single atoms and defective Cu sites on the surface of catalysts, where Au single atoms promote *CO generation and Cu defects stabilize the key intermediate *OCCO, which altogether enhances C−C coupling kinetics. This work provides important insights into the catalyst design for electrochemical CO_2 reduction to multicarbon products.

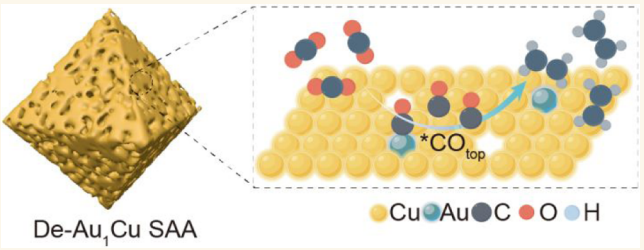

KEYWORDS: *electrochemical CO_2 reduction, nanoporous structure, electrocatalysis, single-atom Au_1Cu alloy, dealloying*

1. INTRODUCTION

Electrocatalytic reduction of CO_2 into valuable chemicals using renewable electricity provides a sustainable method for CO_2 recycling and utilization, which plays a crucial role in achieving a carbon−neutral cycle.[1−3] Over the past decade, remarkable progress has been made toward the generation of single-carbon (C1) products, such as carbon monoxide (CO) and formic acid (HCOOH), through the electrocatalytic CO_2 reduction reaction (CO_2RR).[4−6] However, these C1 products are of limited value for practical applications, compared to multicarbon products (e.g., C2, C3, etc.). For this reason, significant efforts have recently been dedicated to producing multicarbons of higher added values via the CO_2RR.[7−9] Among many CO_2RR electrocatalysts developed so far, copper (Cu) has been demonstrated to be the most important metal catalyst, if not the only, that can effectively catalyze the conversion of CO_2 into multicarbon commodities. Nonetheless, the sluggish C−C coupling kinetics on a pure Cu surface severely hinders the yield of multicarbon products during the CO_2RR.[10,11] To address this challenge, various catalyst design strategies including morphology control,[12−15] surface defect engineering,[16−19] and alloying/doping,[20−24] have been proposed to enhance the electrocatalytic performance of Cu-based catalysts toward multicarbon production, and improved CO_2RR activities were already observed.

In principle, the C−C coupling kinetics are dominated by two factors, namely, the coverage of *CO intermediates on catalyst's surfaces and the binding energy of *CO−*CO dimers.[25,28] Previous studies have demonstrated that when Cu is alloyed with metals showing a high selectivity toward CO generation (e.g., Au and Ag), the CO produced on such metal sites can be

Received: October 3, 2024
Revised: January 1, 2025
Accepted: January 2, 2025
Published: January 24, 2025

https://doi.org/10.1021/acsnano.4c13961
ACS Nano 2025, 19, 4505−4514

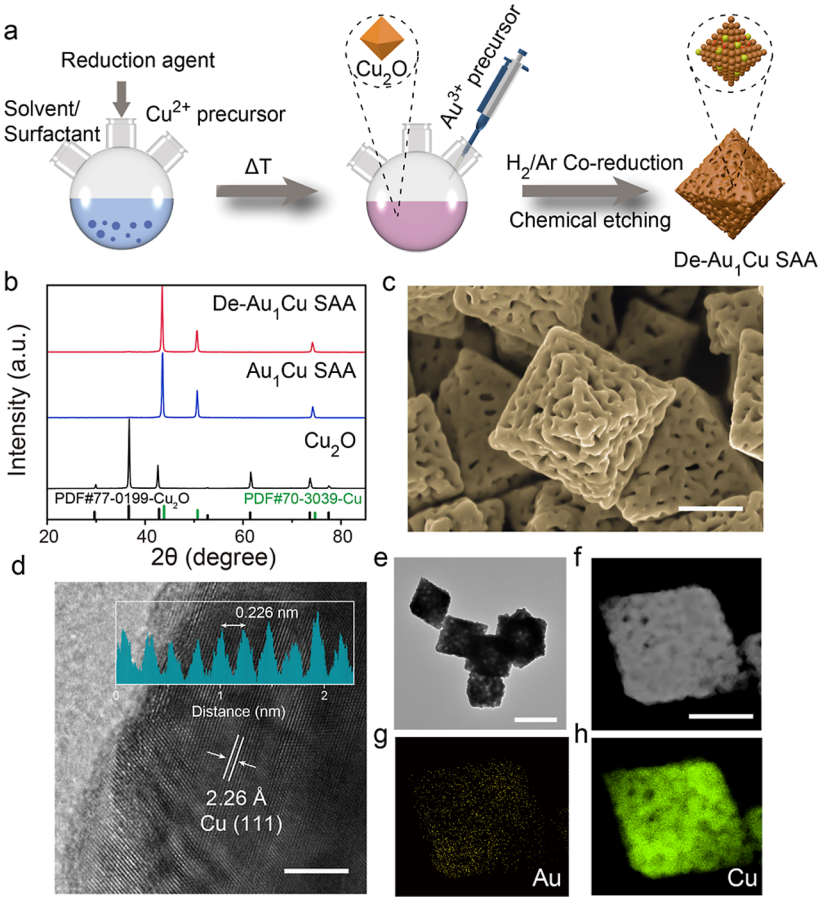

Figure 1. (a) Schematic illustration of the preparation of De-Au$_1$Cu SAA. (b) XRD patterns, (c) SEM image (scale bar: 500 nm), (d) HRTEM image (scale bar: 5 nm), (e) low-magnification TEM image (scale bar: 1 μm), (f) HAADF-STEM image (scale bar: 500 nm), and STEM−EDX elemental maps of (g) Au and (h) Cu. Inset of panel (d): line-scan intensity profile across lattice fringes.

easily transferred to the adjacent Cu sites, facilitating the formation of multicarbons. Obviously, such a cascade catalysis strategy is highly preferred.[29−33] To this end, Chen et al.[34] designed a Cu−Ag tandem catalyst where Ag sites supply sufficient *CO species, which led to a 4-fold increase in C2 production rate compared to the case using Cu alone as the catalyst. Additionally, Liu et al.[35] reported a cascade catalysis strategy to improve the yield of C2 products by loading nickel single-atom catalysts (Ni SACs) on a Cu catalyst. By doing so, they achieved a high selectivity for ethylene (C_2H_4), which was ascribed to the synergistic catalysis of Ni SACs in generating *CO species and facilitating *CO dimerization on the Cu surface. Notwithstanding some progress, the catalyst designs previously reported for cascade CO_2RR mainly focused on improving the surface concentration of adsorbed *CO intermediates, with little emphasis on modulation of the binding energy of *CO dimerization on Cu, though this is an important factor determining the C2 product yield. Recent studies showed that introducing surface metal defects or vacancies is an effective way of optimizing the local electronic structure and generating undercoordinated sites to modulate the binding energy of key reaction intermediates.[36,37] Therefore, combining the inherent advantages of alloying and metal defects engineering is expected to be able to effectively promote the CO_2RR selectivity toward multicarbon products.[26,27]

Bearing these ideas in mind, we herein report the synthesis of nanoporous Au$_1$Cu single-atom alloys (De-Au$_1$Cu SAA) comprising nanoporous (np) defective Cu octahedrons covered with Au single atoms on their surfaces, considering that Au has a high selectivity toward CO generation and introducing Au in the form of single atoms would not significantly increase the cost of electrocatalysts. The as-prepared De-Au$_1$Cu SAA catalyst demonstrates favorable CO_2RR activity and selectivity toward C2 products, exhibiting a 52% Faradaic efficiency for C_2H_4 production, with reasonably good stability of 54 h at a comparatively large current density of 100 mA cm^{-2} in an alkaline flow cell. In situ Fourier-transform infrared spectroscopic characterization and density functional theory (DFT) calculations reveal that there is synergy between Au single-atoms and surface Cu defects, namely, the atomically dispersed Au promotes the activation and conversion of CO_2 molecules to *CO with an optimal concentration, and these surface-adsorbed *CO species are subsequently transferred to adjacent defective Cu sites, making the C−C coupling easier and thereby notably boosting the production of C_2H_4.

2. RESULTS AND DISCUSSION

2.1. Catalyst Preparation and Characterization. The synthesis of De-Au$_1$Cu SAA catalysts is schematically illustrated in Figure 1a. First, octahedral copper(I) oxide (Cu_2O) particles with a dimension of ~800 nm were prepared through a wet chemical reduction method (Figure S1), which acted as the precursors and templates for subsequent synthesis of De-Au$_1$Cu SAA. Afterward, the Cu_2O particles were mixed with $HAuCl_4$ and urea, and the mixture chemically reacted at room temperature. The obtained products were then thermally

https://doi.org/10.1021/acsnano.4c13961
ACS Nano 2025, 19, 4505−4514

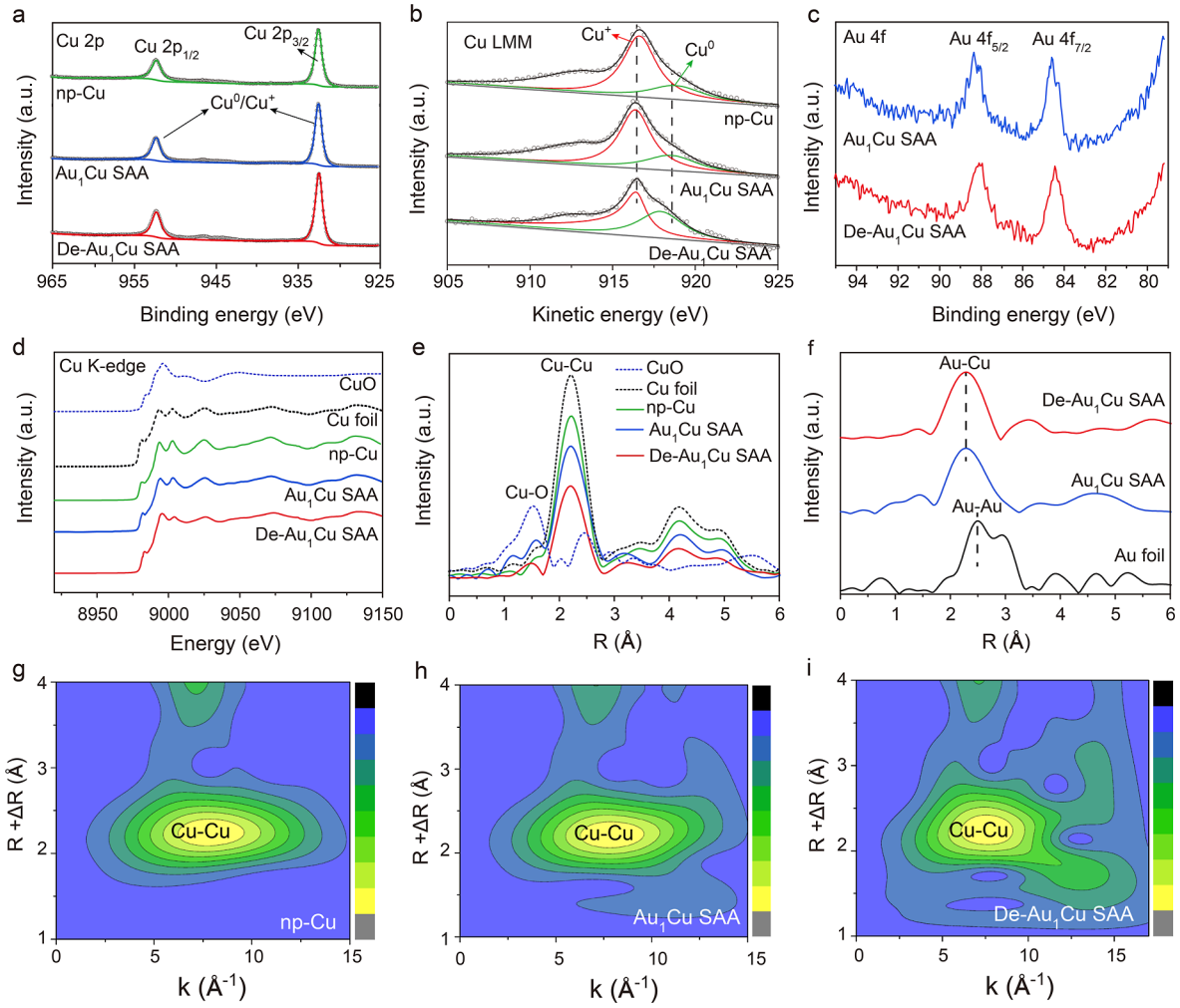

Figure 2. Spectroscopic characterization of De-Au$_1$Cu SAA and control samples. High-resolution (a) Cu 2p XPS, (b) Cu LMM AES, and (c) Au 4f XPS spectra. (d) Cu K-edge XANES spectra and (e) the corresponding FT-EXAFS spectra. (f) FT-EXAFS of Au L$_3$-edge. Wavelet transform contours of (g) np-Cu, (h) Au$_1$Cu SAA, and (i) De-Au$_1$Cu SAA.

treated in a flow of H_2/Ar at 300 °C to reduce Cu_2O into nanoporous Au_1Cu SAA (see Experimental section). Finally, the Au_1Cu SAA was subjected to dealloying treatment in a mild acetic acid to remove extra surface Cu atoms. Upon acid treatment, the color of the solution changed from red to blue (Figure S2), indicating that a portion of Cu atoms were leached out, thereby introducing defective sites. The crystal structures of De-Au_1Cu SAA, Au_1Cu SAA, and Cu_2O precursor particles were examined by X-ray diffraction (XRD). The particles prepared by wet chemical reduction show diffraction peaks at 29.6°, 36.6°, 42.5°, 61.6°, 73.7° and 77.5°, which match well with the (110), (111), (200), (220), (310) and (222) crystal planes of face-centered cubic (fcc) copper(I) oxide (PDF no. 77-0199), confirming that phase-pure Cu_2O was obtained (Figure 1b). After thermal reduction, the Cu_2O precursor particles were completely reduced to metallic Cu, with main diffraction peaks at 43.3°, 50.4° and 74.2°, corresponding to the (111), (200) and (220) facets of fcc Cu (PDF no. 70-3039). There are not any diffraction peaks arising from Au, implying that Au may disperse atomically in the Cu lattice. Moreover, both the dealloying treatment in acetic acid and the presence of Au do not affect the crystal structure of Cu, as evidenced by the fact that the XRD patterns of De-Au_1Cu SAA and Au_1Cu SAA are nearly identical to the nanoporous Cu (np-Cu) obtained by thermal reduction and selective acid etching without the presence of $HAuCl_4$ (Figure S3).

Scanning electron microscopy (SEM) examination revealed that the octahedral shape of particles was well retained in De-Au_1Cu SAA. However, upon acid treatment, bicontinuous nanopores were formed on the entire body of each octahedron (Figure 1c), which are expected to facilitate the mass transport of reactants and products. The np-Cu shows a similar nanoporous octahedral morphology to De-Au_1Cu SAA (Figure S4). Furthermore, transmission electron microscopy (TEM) was carried out, where the nanopores were clearly observed across each individual particle (Figure 1e). High-resolution TEM (HRTEM) image taken near the surface shows well-defined lattice fringes (Figure 1d), and the measured interplanar spacing parallel to the facet is about 0.226 nm, corresponding to the lattice distance of (111) crystal planes, which indicates that the orientation of (111) facets did not deviate during the thermal reduction and subsequent dealloying. This is consistent with the XRD result (Figure 1b), where the (111) diffraction peak is dominant. However, the measured lattice distance is slightly larger than that of (111) planes of pure Cu (~0.21 nm), which can be attributed to the doping of Au atoms having a greater atomic radius into the Cu lattice, causing the lattice expansion. Additionally, the spatial distribution of Au and Cu

https://doi.org/10.1021/acsnano.4c13961
ACS Nano 2025, 19, 4505−4514

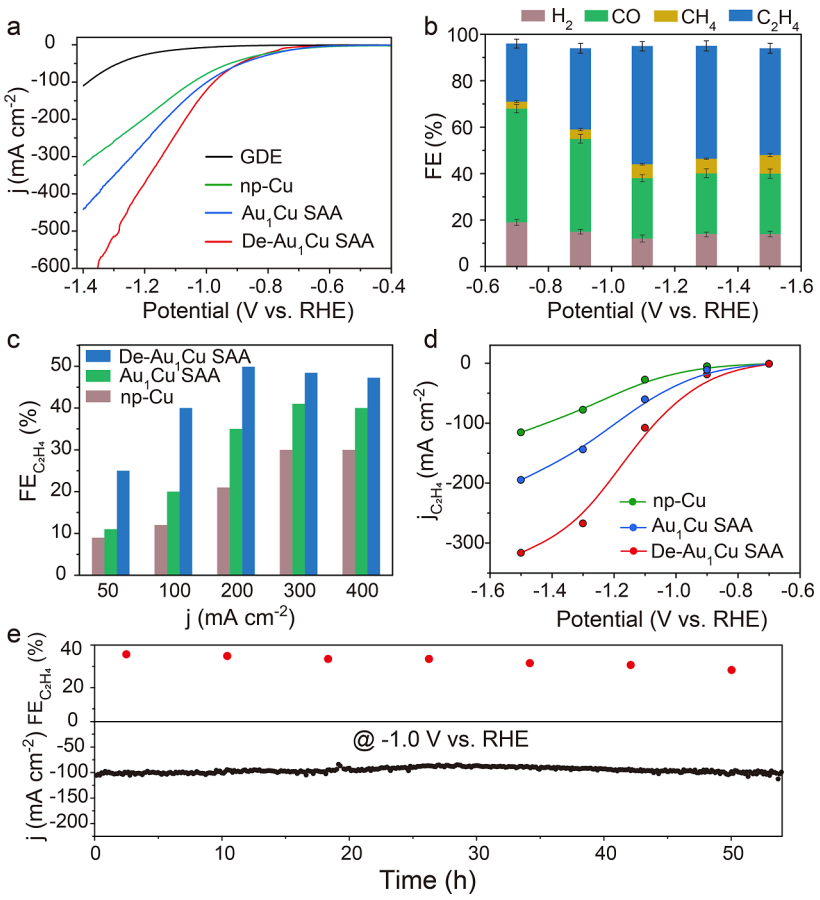

Figure 3. (a) LSV curves of the De-Au_1Cu SAA and control samples. (b) Faradaic efficiency values of H_2, CO, CH_4, and C_2H_4 production for De-Au_1Cu SAA. (c) The FE of C_2H_4 production at various current densities for different catalysts. (d) Partial current density of De-Au_1Cu SAA and control samples toward C_2H_4 production. (e) Long-term stability of the De-Au_1Cu SAA at −1.0 V vs RHE.

was examined by scanning transmission electron microscopy in the high-angle annular dark-field mode (HAADF-STEM, Figure 1f). The signal of Au is weak but appears across the entire octahedron particle (Figure 1g), indicating that Au atoms spread all over the particle though their percentage in De-Au_1Cu SAA is little. Interestingly, the nanoporous morphology can also be clearly observed in the Cu map (Figure 1h). Besides, nitrogen adsorption/desorption isotherms of all samples were measured at 77 K (Figure S5), and the results show that De-Au_1Cu SAA has the highest specific surface area of 15.4 $m^2 g^{-1}$ relative to np-Cu and Au_1Cu SAA, though the pore size distribution of these samples is similar.

The surface chemistry and coordination structure of the De-Au_1Cu SAA were further examined by X-ray photoelectron spectroscopy (XPS) and X-ray absorption spectroscopy (XAS). Two binding energy (BE) peaks are observed at 932.5 and 952.4 eV in the high-resolution Cu 2p XPS spectra of all samples (Figure 2a), which correspond to the Cu $2p_{3/2}$ and Cu $2p_{1/2}$ components of Cu^0/Cu^+ species, respectively.[38] Since it is very difficult to distinguish Cu^0 from Cu^+ species in Cu 2p XPS spectrum, the Cu LMM Auger electron spectroscopy (AES) was further analyzed (Figure 2b). Upon peak fitting, two characteristic components are found at 916.8 and 918.6 eV, which can be assigned to Cu^0 and Cu^+,[39,40] respectively, with Cu^+ species being dominant. Considering that the above XRD and TEM results do not show the presence of Cu_2O, it is believed that the Cu^+ species only exist on the outermost surface, which arise from the exposure of samples to air before examination.[41] Furthermore, Au 4f XPS spectra of Au_1Cu SAA and De-Au_1Cu SAA were also acquired, and the Au $4f_{7/2}$ and Au $4f_{5/2}$ components appear at 84.4 and 88.1 eV (Figure 2c), respectively, consistent with those observed in the $AuCu_{19}$ alloy previously.[42]

Raman spectroscopy characterization was further carried out for De-Au_1Cu SAA, np-Cu, and Cu_2O particles. Two Raman bands located at 218 and 635 cm^{-1} appeared for Cu_2O particles (Figure S6), characteristic of the Cu_2O phase.[16] In contrast, there was no Raman signal observed for both De-Au_1Cu SAA and np-Cu, indicating that they are in metallic state and not Raman-active. Furthermore, synchrotron X-ray absorption spectroscopy (XAS) was used to investigate the electronic structure and local coordination environment of catalysts. The Cu K-edge X-ray absorption near-edge structure (XANES) spectra of np-Cu, Au_1Cu SAA and De-Au_1Cu SAA are quite similar to that of the Cu foil (Figure 2d), suggesting that Cu^0 dominates in these samples. The Fourier transform extended X-ray absorption fine-structure (FT-EXAFS) spectra of De-Au_1Cu SAA, Au_1Cu SAA and np-Cu all show a main signal at ~2.4 Å that is assigned to Cu−Cu bonding, and there is a lack of the Cu−O bonding signal (~1.5 Å, Figure 2e and Table S1), which confirms the predominance of metallic Cu in De-Au_1Cu SAA. Moreover, the intensity of Cu−Cu signal is the weakest for De-Au_1Cu SAA, manifesting its highly defective nature. The EXAFS fitting results further reveal that the coordination number (CN) of Cu in De-Au_1Cu SAA is 6.7 ± 0.9 (Figure S7 and Table S1), smaller than that in Au_1Cu SAA (7.1 ± 0.8) and np-Cu (7.6 ±

https://doi.org/10.1021/acsnano.4c13961
ACS Nano 2025, 19, 4505−4514

0.5), quantitatively corroborating the formation of low-coordination defective Cu sites.[38,43] In addition, the Au L_3-edge XANES and FT-EXAFS spectra of Au_1Cu SAA and De-Au_1Cu SAA were also acquired. The absorption edge of both samples overlaps with that of the Au foil (Figure S8), suggesting that the Au in Au_1Cu SAA and De-Au_1Cu SAA is essentially in the metallic state. Moreover, both Au_1Cu SAA and De-Au_1Cu SAA exhibit a prominent peak at ~2.27 Å that can be assigned to Au−Cu bonding (Figure 2f), and no signal appears at ~2.52 Å, typical of Au−Au bonding. This clearly demonstrates that Au is dispersed in the catalyst atomically, forming the SAA.[44,45] Furthermore, the wavelet transform (WT) of Cu K-edge EXAFS oscillations is plotted (Figure 2g−i). The intensity maxima of np-Cu appears at ~8.1 $Å^{-1}$, which can be attributed to the Cu−Cu coordination. In contrast, the WT contour plots of Au_1Cu SAA and De-Au_1Cu SAA display a maximal intensity at ~7.8 and ~7.4 $Å^{-1}$, respectively, implying the formation of defects in both, more prominently in De-Au_1Cu SAA. The XAS investigation unambiguously demonstrates the atomic dispersion of Au in De-Au_1Cu SAA and the highly defective nature of De-Au_1Cu SAA.

2.2. Electrocatalytic CO_2RR Performance. The electrocatalytic CO_2RR performance of the De-Au_1Cu SAA was evaluated in an alkaline (1.0 M KOH) flow cell with a gas-diffusion electrode (GDE, Figure S9). The calibration curves for gas chromatography (GC) and the representative gas-phase products of CO_2RR catalyzed by De-Au_1Cu SAA are shown in Figures S10 and S11. For comparison, the CO_2RR performance of np-Cu and Au_1Cu SAA was also measured. Before comprehensive electrochemical assessment, the influence of Au loading in dealloyed Au−Cu SAA on CO_2RR performance was first appraised. Benchmarked with the Faradaic efficiency (FE) toward C_2H_4 generation (Figure S12), the optimal Au loading was identified to be ~1 wt % (the sample denoted as De-Au_1Cu SAA, unless otherwise specified), according to the inductively coupled plasma optical emission spectrometry (ICP-OES) measurements (Table S2). The optimized dealloyed Au−Cu SAA (i.e., De-Au_1Cu SAA) was then used in subsequent detailed electrocatalytic evaluation. Figure 3a exhibits the linear sweep voltammetry (LSV) curves of all catalysts and the pristine GDE. Without loading any catalysts, the GDE shows a negligible cathodic current density until −1.2 V vs reversible hydrogen electrode (RHE). In contrast, after catalyst loading, the CO_2RR onset potential is significantly reduced. Particularly, the cathodic current density of De-Au_1Cu SAA quickly reaches 600 mA cm^{-2} at −1.35 V vs RHE under a constant CO_2 flow, suggesting the superior CO_2RR activity of De-Au_1Cu SAA. The FE values of De-Au_1Cu SAA toward different products are plotted against the applied potential (Figure 3b), where it is seen that the FE of CO production decreases and that of C_2H_4 production rises up as the applied cathodic potential increases. Specifically, the FE of C_2H_4 generation amounts to a maximal value of (52 ± 1.8)% at −1.1 V vs RHE, favorably comparing to that of other Cu-based CO_2RR SAA electrocatalysts reported in the literature (Table S3). Figure 3c illustrates the FE values of C_2H_4 production at various current densities ranging from 50 to 400 mA cm^{-2}, where De-Au_1Cu SAA shows substantially better performance than np-Cu and Au_1Cu SAA controls. Figure S13 further compares the FE values of CO and H_2 production for all samples at different current densities. The FE of CO production decreases as the current density increases, suggesting that at high current densities, CO species are prone to undergoing coupling to form C2 products. Particularly, np-Cu shows the highest CO selectivity (Figure S13a), which reasonably explains why the FE of np-Cu for C2 product formation is low. As for H_2 production, the FE values show a declining trend as the current density increases up to 300 mA cm^{-2} (Figure S13b). At 400 mA cm^{-2}, the FE for both np-Cu and Au_1Cu SAA becomes increasing, whereas that for De-Au_1Cu SAA remains relatively stable, indicating that De-Au_1Cu SAA can effectively suppress H_2 evolution at high current densities, which is a key factor enabling better CO_2RR performance. Furthermore, the partial current density of C_2H_4 production on De-Au_1Cu SAA notably exceeds that of both np-Cu and Au_1Cu SAA, showing a remarkable value of >300 mA cm^{-2} at −1.5 V vs RHE (Figure 3d).

To gain insight into the higher performance dictated by De-Au_1Cu SAA, the CO_2 adsorption capability of different catalysts was assessed. The De-Au_1Cu SAA catalyst exhibits significantly higher CO_2 adsorption capability than np-Cu and Au_1Cu SAA (Figure S14), which may lead to CO_2 enrichment near the local electrode surfaces, enhancing CO_2 adsorption and activation.[46,47] The capability of *CO desorption from different catalysts was also investigated by the electrochemical CO stripping voltammetry (Figure S15). The *CO species begin to desorb from the np-Cu surface at a much earlier potential of 0.69 V vs RHE (@0.5 mA cm^{-2}), manifesting that *CO can be easily removed from np-Cu. In contrast, the *CO desorption starts at 0.77 and 0.79 V vs RHE, respectively, for Au_1Cu SAA and De-Au_1Cu SAA, which suggests that the introduction of Au single atoms and defective sites hinders *CO desorption, making adsorbed *CO species have sufficient time and chance to couple with each other forming C2 products. Additionally, the electrochemically active surface area (ECSA) was determined based on the double-layer capacitance (C_{dl}) method (Figure S16). Notably, the De-Au_1Cu SAA catalyst shows the highest ECSA value (330 cm^2) among all samples, suggesting that it may expose more active sites that contribute to the higher activity. Furthermore, electrochemical impedance spectroscopy (EIS) measurements were performed to analyze the interfacial charge transfer processes (Figure S17). The De-Au_1Cu SAA exhibits the lowest charge transfer resistance (R_{ct}) among all catalysts (Table S4), indicating that rapid electron transfer occurs at the catalyst/electrolyte interface, which results in accelerated CO_2RR kinetics. In addition, the long-term stability of the De-Au_1Cu SAA catalyst toward CO_2RR was evaluated under a fixed potential of −1.0 V vs RHE (Figure 3e). Impressively, the De-Au_1Cu SAA could continuously catalyze CO_2RR at ~100 mA cm^{-2} with ~40% C_2H_4 FE for 54 h with minimal degradation, showing outstanding catalytic stability. To inspect whether the morphology and surface chemistry of De-Au_1Cu SAA changed after the long-term stability test, SEM, TEM, and XPS analyses were conducted. SEM examination revealed that the octahedral morphology was well retained in the postelectrolysis sample, without any sign of structural collapse (Figure S18). Some flake-like fine structure appears around the octahedral particles, which may result from bicarbonate side products introduced during the reaction. TEM inspection further confirmed the intactness of De-Au_1Cu SAA octahedral particles, and the nanoporous morphology could still be clearly discerned (Figure S19a). HRTEM imaging also corroborated that the crystalline structure of De-Au_1Cu SAA remained after the extended stability test, and the lattice fringes of (111) crystal planes were distinctly visible (Figure S19b). Besides, XPS examination showed no discernible changes in the binding energy peaks of Cu 2p and Au 4f components for De-Au_1Cu SAA before and after the stability test, suggesting that the surface chemistry of De-Au_1Cu SAA was

https://doi.org/10.1021/acsnano.4c13961
ACS Nano 2025, 19, 4505−4514

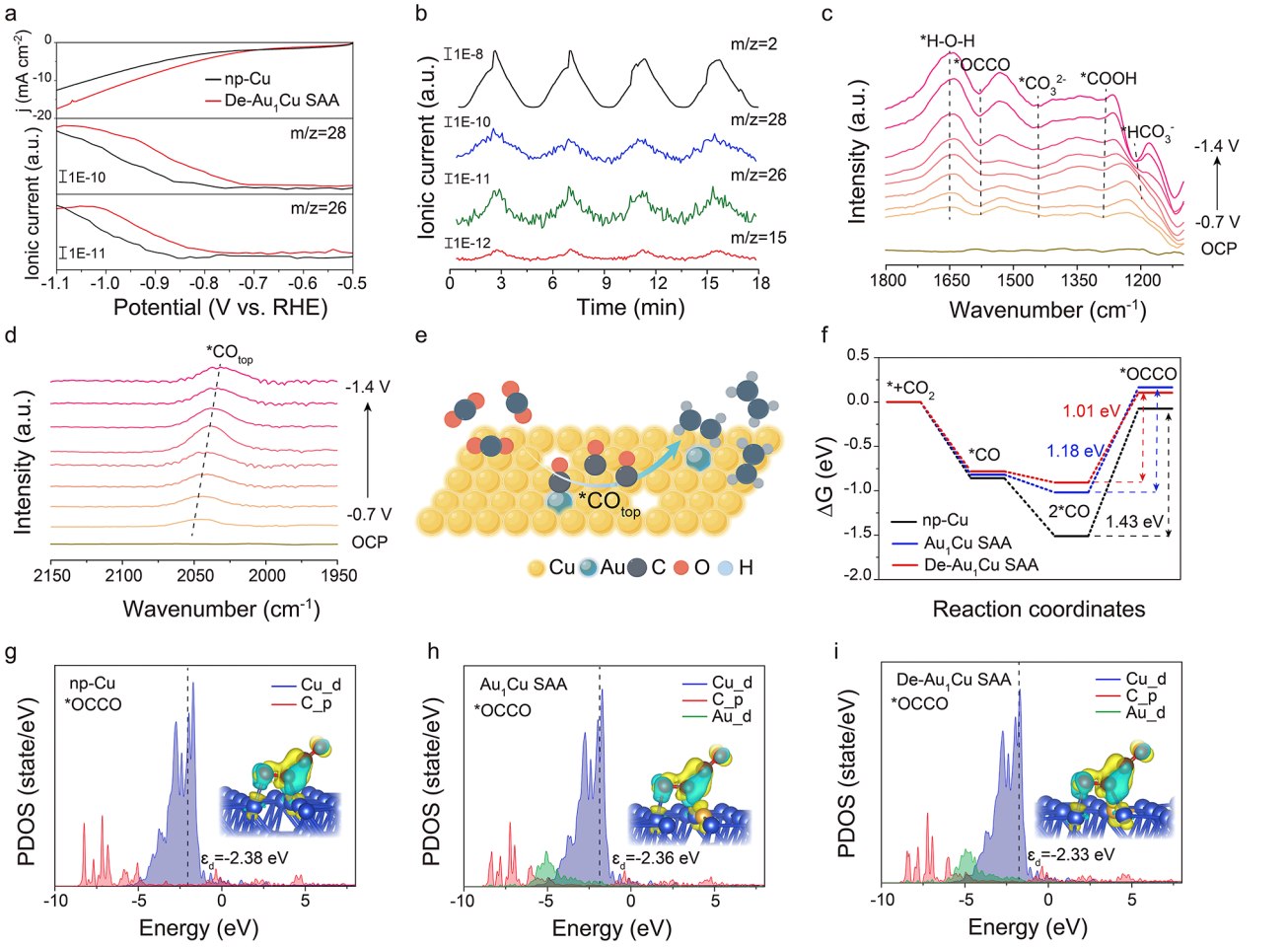

Figure 4. (a) In situ DEMS measurement of CO (m/z = 28) and C_2H_4 (m/z = 26) production during the CO_2RR on np-Cu and De-Au$_1$Cu SAA. (b) DEMS analysis of De-Au$_1$Cu SAA in consecutive CV cycles. (c,d) In situ ATR-SEIRAS spectra of De-Au$_1$Cu SAA acquired at various potentials from −0.7 to −1.4 V vs RHE. (e) Schematic illustration of CO_2 conversion into C_2H_4 over the De-Au$_1$Cu SAA catalyst. (f) Diagrams showing the free energy changes during different reaction steps on the catalysts. PDOS of *OCCO-adsorbed surfaces of (g) np-Cu, (h) Au$_1$Cu SAA, and (i) De-Au$_1$Cu SAA. The inset shows the corresponding charge density difference maps (the cyan and yellow regions denote electron depletion and electron accumulation, respectively. The red, gray, yellow and blue spheres represent O, C, Au, and Cu atoms, respectively, in all models).

not significantly altered during the CO_2RR (Figure S20). However, upon a close look into the Cu LMM Auger spectrum, a distinct peak at 567.6 eV that can be assigned to Cu^0 appears, and the intensity of Cu^+ component accordingly decreases, which indicates that the surface Cu^+ species was reduced to metallic Cu after the long-term CO_2RR. The above post-mortem analyses reaffirm the outstanding catalytic stability of the De-Au$_1$Cu SAA catalyst, making it a promising candidate for future applications.

2.3. Mechanistic Investigation of the CO_2RR on De-Au$_1$Cu SAAs. In pursuit of a molecular-level understanding of the CO_2-to-C_2H_4 conversion pathway, in situ differential electrochemical mass spectrometry (DEMS, Figure S21) was carried out to analyze the reaction intermediates. Figure 4a depicts the LSV curves and the corresponding changes of m/z signals associated with CO (m/z = 28) and C_2H_4 (m/z = 26) fragments during the CO_2RR. The De-Au$_1$Cu SAA catalyst exhibits a lower onset potential for both CO and C_2H_4 generation, compared to np-Cu, which indicates that alloying Au with Cu indeed enhances intrinsic activity and selectivity, thereby promoting C_2H_4 formation. Moreover, consecutive cyclic voltammetry (CV) was performed in the potential range of −0.6 V to −1.4 V vs RHE while synchronously coupling with DEMS measurements (Figure 4b). All gaseous products including H_2, C_2H_4, CO and CH_4, were detected at m/z = 2, 26, 28 and 15, respectively, throughout the CV cycles, consistent with the above GC results. It is worth noting that the CO mass signal was initially high and then showed a slight decrease as C_2H_4 emerged, indicating that CO is an essential intermediate in the production of C_2H_4.[35,40] Besides, in situ attenuated total reflectance surface-enhanced infrared absorption spectroscopy (ATR-SEIRAS) was also performed to dynamically monitor the *CO coverage on De-Au$_1$Cu SAA during the CO_2RR (Figure S22). Figure 4c shows a series of SEIRAS spectra acquired at different potentials from the open circuit potential (OCP) to −1.4 V vs RHE on De-Au$_1$Cu SAA in CO_2-saturated 0.5 M $KHCO_3$. The bands located at ∼1646, ∼1446 and ∼1221 cm^{-1} were detected once the cathodic potential was applied, which arise from the vibration of water (*H−O−H) molecules and carbonate species (i.e., $*CO_3^{2-}$ and $*HCO_3^-$) in the electrolyte.[48,49] The band at ∼1295 cm^{-1} can be assigned to the C−OH stretching mode from *COOH, which is identified as a typical intermediate for *CO generation.[50,51] As the cathodic bias increases, the peak at ∼1576 cm^{-1}, corresponding to the

https://doi.org/10.1021/acsnano.4c13961
ACS Nano 2025, 19, 4505−4514

asymmetric vibration of *OCCO, emerges as a crucial intermediate for C_2H_4 production.[52,53] Figure 4d displays the SEIRAS spectra in the spectral range of atop-adsorbed *CO (*CO_{top}) vibrational modes (i.e., 2010−2075 cm^{-1}). Throughout the entire potential window applied, the *CO_{top} band frequency redshifts as the applied cathodic potential increases due to the Stark effect.[35,54] Interestingly, the intensity of *CO_{top} peak first increases and then decreases with the increasing cathodic potential. Considering the constantly increased intensity of the *OCCO signal with the increasing cathodic potential (Figure 4c), this suggests fast *CO consumption owing to the C−C coupling. By contrast, the *CO_{top} coverage on the surface of pristine np-Cu was only observed at a large cathodic potential (Figure S23), which confirms that the presence of Au single atoms and Cu defects can indeed more effectively promote CO dimerization reaction (Figure 4e).

To gain further insight into the synergetic effect between the Au single atoms and Cu defective sites during the CO_2RR, DFT calculations were conducted. Given that the (111) facet prevails in the octahedral catalyst particles (Figure 1), model catalysts including np-Cu (111), Au_1Cu (111) SAA, and defective De-Au_1Cu (111) SAA were constructed (see Experimental details, Figure S24). Typically, the *CO + *CO → *OCCO step is the rate-determining step (RDS) toward the production of C2 products, especially at high potentials.[55,56] As shown in Figure 4f, the Gibbs energy change (ΔG) of the RDS on De-Au_1Cu SAA is 1.01 eV, notably smaller than that of Au_1Cu SAA (1.18 eV) and np-Cu (1.43 eV), suggesting that the introduction of Cu defects to Au_1Cu SAA can lower the energy barrier of the C−C coupling and that the Cu defects work synergistically with Au single atoms reducing the energy barrier to the RDS (as compared to the np-Cu) during the CO_2RR. Moreover, the adsorption energy of *OCCO on De-Au_1Cu SAA is calculated to be −0.34 eV (Figure S25), which falls in between that of Au_1Cu SAA (−0.26 eV) and np-Cu (−0.50 eV). The moderate binding strength of the key intermediate *OCCO is favorable for subsequent hydrogenation on De-Au_1Cu SAA and the release of C_2H_4, compared to the too strong adsorption on np-Cu and too weak adsorption on Au_1Cu SAA. In order to estimate the binding affinity to *OCCO, the projected density of states (PDOS) of the bare surfaces of different model catalysts were further calculated (Figure 4g−i). An upshift of the Cu d-band center toward the Fermi level was observed for the De-Au_1Cu SAA (−2.33 eV), as compared to that of the Au_1Cu SAA (−2.36 eV) and np-Cu (−2.38 eV), which suggests stronger interaction of the De-Au_1Cu SAA with the key intermediate *OCCO. Moreover, the PDOS of Cu d orbital of the De-Au_1Cu SAA shows a larger overlap with that of the Au d orbital and *OCCO p orbital, reaffirming the stronger electronic interaction and binding force of *OCCO species with the defective, Au single-atom modified Cu surface. The adsorption behavior of the *OCCO intermediate on different Cu active sites was further investigated using the charge density difference analysis. As shown in the insets of Figure 4g−i, a large change in electron cloud distribution is observed when *OCCO is adsorbed on the catalyst surface. In particular, the charge density difference of the *OCCO intermediate shows stronger charge interactions at the defective Cu−Au interface in De-Au_1Cu SAA (Figure 4i inset). This differs from np-Cu and Au_1Cu SAA, which indicates that the defective Cu−Au surface, as a catalytically more active site, can better stabilize the *OCCO intermediate. Besides, the PDOS of different model catalysts adsorbed with 2 *CO intermediates was also computed (Figure S26), and De-Au_1Cu SAA also exhibits stronger interaction with two neighboring *CO species than np-Cu and Au_1Cu SAA, implying that the adsorbed neighboring *CO species have more chance to couple with each other forming C2 products on De-Au_1Cu SAA. Overall, our DFT calculations firmly support the experimental observations, highlighting the important role of Au single atoms and the Cu defects in boosting the CO_2RR performance toward the production of C2 products.

3. CONCLUSIONS

In summary, a nanoporous defective Au_1Cu single-atom alloy (De-Au_1Cu SAA) electrocatalyst was designed and successfully synthesized. When used to catalyze the electrochemical CO_2RR, the De-Au_1Cu SAA catalyst exhibits good selectivity toward the production of C_2H_4, with a Faradaic efficiency of 52% at the current density of 252 mA cm^{-2} under −1.1 V vs RHE. Comprehensive in situ spectroscopic studies confirmed that *CO is an important intermediate species and the presence of Au single atoms and Cu defects facilitate the dimerization of *OCCO. DFT calculations further validate the role of Cu defects and Au single atoms in promoting the CO_2 conversion to C2 product. It is believed that the atomically dispersed Au boosts the activation and conversion of CO_2 molecules to *CO species with an optimal concentration, which are subsequently transferred to the adjacent defective Cu site for C−C coupling. Our work provides important insights into the tandem catalysis process occurring in Au_1Cu SAA catalysts and offers useful guideline for catalyst design toward the production of multicarbon commodities during the CO_2RR.

4. EXPERIMENTAL SECTION

4.1. Preparation of Cu_2O(111) Octahedrons. The Cu_2O octahedrons were synthesized through a wet chemical reduction method reported previously with slight modification.[57] In a typical synthesis, 1 mmol of $CuCl_2·2H_2O$ was dissolved in 100 mL of DI water. Subsequently, 3.5 g of PVP (MW: 30,000−40,000) were introduced into the solution. Next, 10.0 mL of NaOH aqueous solution (2.0 M) were added dropwise to the mixture. After stirring for 30 min, 10.0 mL of ascorbic acid solution (0.6 M) were added dropwise to the dark brown solution. The mixture was then aged for 3 h, during which its color gradually turned to red and turbid. The entire procedure was conducted under constant stirring at 55 °C in a water bath. The resulting precipitates were collected by centrifugation and decanting, washed three times with DI water and another three times with dehydrated ethanol, and finally dried under vacuum at 60 °C for 6 h.

4.2. Preparation of Au_1Cu(111) Single-Atom Alloys. The Au_1Cu SAA exposed with Cu(111) facets were synthesized using the H_2-reduction method. Initially, 100 mg of Cu_2O powders were added to 100 mL of DI water. Subsequently, a mixed solution containing $HAuCl_4$ (1.0, 2.5, and 5.0 wt % of the Cu_2O mass, respectively) and urea (20 wt % of the Cu_2O mass) was introdcued and left to react with Cu_2O at 25 °C for 3 h. Next, the H_2-reduction process was carried out at 300 °C for 60 min on the formed Au^{3+}/Cu_2O in a flow of 5 vol % H_2/Ar at ambient pressure to produce nanoporous (np) Au_1Cu SAA. For comparison, a control catalyst consisting of nanoporous Cu (np-Cu) was also prepared by direct H_2 reduction of Cu_2O particles without the presence of any gold salt.

4.3. Preparation of De-Au_1Cu(111) Single-Atom Alloys. The obtained Au_1Cu (111) SAA materials were dispersed in 10 mL of acetic acid (CH_3COOH) and heated to 40 °C. After stirring for 1 h, the resulting defective Au_1Cu SAA (i.e., De-Au_1Cu SAA) product was centrifuged, washed with DI water, and dried under vacuum.

4.4. Materials Characterization. The morphology of Cu-based catalysts was characterized by field-emission scanning electron microscopy (FE-SEM, ZEISS/Gemini 300) equipped with an energy-dispersive X-ray spectrometer (EDX, Oxford). Powder X-ray diffraction

https://doi.org/10.1021/acsnano.4c13961
ACS Nano 2025, 19, 4505−4514

(XRD) examinations were conducted using an Aeris instrument (Malvern Panalytical) operating at 40 kV and 15 mA with Cu Kα radiation (λ = 1.5406 Å). X-ray photoelectron spectroscopy (XPS) characterization was performed on an ESCALAB 250Xi instrument with an Al Kα X-ray source (1486.6 eV). The specific surface area was determined by N_2 adsorption/desorption isotherms acquired at 77 K (Quantachrome Autosorb IQ2) using the Brunauer−Emmet−Teller (BET) method. The content of Au/Cu in the catalysts was quantified using inductively coupled plasma-optical emission spectrometer (ICP-OES, Thermo Scientific 7200). Transmission electron microscopy (TEM) and EDX mapping were conducted on a transmission electron microscope operating at 200 kV (JEOL, JEM-F200). The X-ray absorption spectroscopy (XAS) measurements were conducted at the ASTRA beamline, SOLARIS National Synchrotron Radiation Centre in Krakow, Poland.

4.5. Electrocatalytic Measurements. All electrochemical CO_2RR experiments were conducted in a commercial flow cell separated by an anion exchange membrane (PiperION-A20). Each compartment was filled with 50 mL of 1 M KOH electrolyte. A Pt foil and a Hg/HgO electrode served as the counter and reference electrodes, respectively. All electrode potentials are converted to the RHE scale using the formula $E_{RHE} = E_{Hg/HgO} + 0.098\ V + 0.0591 \times pH$. 85% *iR* correction was applied to compensate the *iR* drop between the working electrode and the reference electrode. Linear sweep voltammetry (LSV) curves were recorded using a CS-310MA electrochemical workstation at a scan rate of 10 mV s^{-1}. Chronoamperometry (CA) or chronopotentiometry (CP) tests were conducted at each potential/current density for 20 min. Current densities were normalized to the geometric surface area of the electrode (i.e., 1 cm^{-2}). CO_2 gas was delivered into the cathodic compartment at a rate of 30 sccm and injected online into a gas chromatograph (GC, BFRL-SP-3530). The catalyst was loaded onto a gas diffusion electrode (YLS-30T, Suzhou Sinero Company) with a loading mass of 2 mg cm^{-2}. For the long-term stability test, the gas diffusion electrode (GDE) was prepared by spraying a PTFE dispersion (DISP-30, DuPont) onto the gas diffusion layer with a loading of ∼1 mg/cm^2. The coated GDE was annealed in a muffle furnace at 380 °C for 30 min in air for further use.

To investigate the desorption capability of different catalysts for *CO intermediates, electrochemical CO stripping voltammetry was carried out. To do so, high-purity CO gas (99.999%) was flowed into the electrolyte (0.1 M H_2SO_4) for 5 min under a bias of 0.1 V vs RHE. Afterward, the electrolyte was repurged with high-purity Argon (Ar, 99.999%) to remove all dissolved CO before CO stripping experiment was performed.

The gaseous products (H_2, CO, C_2H_4 and CH_4) were quantified by a GC (BFRL-SP3530) equipped with a flame ionization detector (FID) for CO, C_2H_4 and CH_4, and a thermal conductivity detector (TCD) for H_2 quantification. High-purity Ar (99.999%) was used as the carrier gas. The Faradaic efficiency of each gaseous product was calculated by the following equation

$$FE\ (\%) = \frac{nzF}{Q} \times 100\% \quad (1)$$

where *n* is the mole fraction of the product, *z* stands for the number of electrons transferred for the product formation, *F* is the Faraday constant, and *Q* represents the total charge passed.

ASSOCIATED CONTENT

Supporting Information

The Supporting Information is available free of charge at https://pubs.acs.org/doi/10.1021/acsnano.4c13961.

Supplementary methods; SEM image of Cu_2O octahedra; XRD and SEM examination results of np-Cu; N_2 adsorption/desorption isotherms of samples; Raman spectra and supplementary XAS data of samples; scheme of flow cells; calibration data of GC; Supporting Information of Faradaic efficiencies of various samples; CO_2 adsorption data; cyclic voltammetry data; EIS Nyquist plots; SEM, EDS, and TEM data of De-Au_1Cu SAA after the stability test; schemes illustrating the configurations of DEMS and ATR-SEIRAS measurements; in situ ATR-SEIRAS spectra of np-Cu; models used for DFT calculations; PDOS of 2*CO-adsorbed surfaces of different samples; tables summarizing the EXAFS fitting, ICP-OES, and EIS fitting data; table comparing the CO_2RR performance of SAA catalysts reported in the literature (PDF)

AUTHOR INFORMATION

Corresponding Authors

Miao Liu − *Songshan Lake Materials Laboratory (SLAB), Dongguan 523808, P. R. China; Institute of Physics, Chinese Academy of Sciences, Beijing 100090, P. R. China*; Email: mliu@sslab.org.cn

Lifeng Liu − *Songshan Lake Materials Laboratory (SLAB), Dongguan 523808, P. R. China*; orcid.org/0000-0003-2732-7399; Email: liu.lifeng@sslab.org.cn

Authors

Yang Zhao − *Songshan Lake Materials Laboratory (SLAB), Dongguan 523808, P. R. China; Institute of Physics, Chinese Academy of Sciences, Beijing 100090, P. R. China*

Yanan Wang − *Songshan Lake Materials Laboratory (SLAB), Dongguan 523808, P. R. China*; orcid.org/0000-0002-8436-0374

Zhipeng Yu − *Songshan Lake Materials Laboratory (SLAB), Dongguan 523808, P. R. China*; orcid.org/0000-0002-3208-649X

Chao Song − *Songshan Lake Materials Laboratory (SLAB), Dongguan 523808, P. R. China*

Jingwei Wang − *Songshan Lake Materials Laboratory (SLAB), Dongguan 523808, P. R. China; Institute of Physics, Chinese Academy of Sciences, Beijing 100090, P. R. China*

Haoliang Huang − *Songshan Lake Materials Laboratory (SLAB), Dongguan 523808, P. R. China*; orcid.org/0000-0002-0993-1536

Lijian Meng − *Centre of Innovation in Engineering and Industrial Technology, Instituto Superior de Engenharia do Porto, Instituto Politecnico do Porto, 4249-015 Porto, Portugal*

Complete contact information is available at: https://pubs.acs.org/10.1021/acsnano.4c13961

Author Contributions

‖Y.Z., Y.W. contributed equally. Y. Zhao: Conceptualization, Investigation, Formal analysis, Writing—original draft. Y. Wang: DFT calculations, Data curation, Funding acquisition, Validation. Z. Yu: XAS measurements, Formal analysis. C. Song: Formal analysis. J. Wang: Formal analysis. H. Huang: XAS analysis, Data curation. L. J. Meng: Formal analysis. M. Liu: Resources, Supervision, Writing—review and editing. L. Liu: Conceptualization, Validation, Project administration, Supervision, Funding acquisition, Writing—review &editing.

Notes

The authors declare no competing financial interest.

ACKNOWLEDGMENTS

L.L. acknowledges the financial support from the Ministry of Science and Technology of China through the Talent Recruitment Programme (grant no. 22J4021Z311) and the start-up grant of the Songshan Lake Materials Laboratory (grant

no. Y2D1051Z311). Y.W. acknowledges the financial support from the National Natural Science Foundation of China (grant no. 12304264). The authors thank Dr. Alexey Maximenko at the ASTRA beamline, SOLARIS synchrotron radiation facility in Poland, for his assistance in XAS experiments.

REFERENCES

(1) De Luna, P.; Hahn, C.; Higgins, D.; Jaffer, S. A.; Jaramillo, T. F.; Sargent, E. H. What would it take for renewably powered electrosynthesis to displace petrochemical processes? *Science* **2019**, *364* (6438), No. eaav3506.

(2) Tackett, B. M.; Gomez, E.; Chen, J. G. Net reduction of CO_2 via its thermocatalytic and electrocatalytic transformation reactions in standard and hybrid processes. *Nat. Catal.* **2019**, *2* (5), 381−386.

(3) Birdja, Y. Y.; Pérez-Gallent, E.; Figueiredo, M. C.; Göttle, A. J.; Calle-Vallejo, F.; Koper, M. T. M. Advances and challenges in understanding the electrocatalytic conversion of carbon dioxide to fuels. *Nat. Energy* **2019**, *4* (9), 732−745.

(4) Qiao, J.; Liu, Y.; Hong, F.; Zhang, J. A review of catalysts for the electroreduction of carbon dioxide to produce low-carbon fuels. *Chem. Soc. Rev.* **2014**, *43* (2), 631−675.

(5) Wang, G. X.; Chen, J. X.; Ding, Y. C.; Cai, P. W.; Yi, L. C.; Li, Y.; Tu, C. Y.; Hou, Y.; Wen, Z. H.; Dai, L. M. Electrocatalysis for CO_2 conversion: From fundamentals to value-added products. *Chem. Soc. Rev.* **2021**, *50* (8), 4993−5061.

(6) Li, M.; Garg, S.; Chang, X.; Ge, L.; Li, L.; Konarova, M.; Rufford, T. E.; Rudolph, V.; Wang, G. Toward excellence of transition metal-based catalysts for CO_2 electrochemical reduction: An overview of strategies and rationales. *Small Methods* **2020**, *4* (7), 2000033.

(7) Zheng, Y.; Vasileff, A.; Zhou, X.; Jiao, Y.; Jaroniec, M.; Qiao, S. Z. Understanding the roadmap for rlectrochemical reduction of CO_2 to multi-carbon oxygenates and hydrocarbons on copper-based catalysts. *J. Am. Chem. Soc.* **2019**, *141* (19), 7646−7659.

(8) Fan, L.; Xia, C.; Yang, F. Q.; Wang, J.; Wang, H. T.; Lu, Y. Y. Strategies in catalysts and electrolyzer design for electrochemical CO_2 reduction toward C_{2+} products. *Sci. Adv.* **2020**, *6* (8), No. eaay3111.

(9) You, S.; Xiao, J.; Liang, S.; Xie, W.; Zhang, T.; Li, M.; Zhong, Z.; Wang, Q.; He, H. Doping engineering of Cu-based catalysts for electrocatalytic CO_2 reduction to multi-carbon products. *Energy Environ. Sci.* **2024**, *17*, 5795−5818.

(10) Cao, B.; Li, F.-Z.; Gu, J. Designing Cu-based tandem catalysts for CO_2 electroreduction based on mass transport of CO Intermediate. *ACS Catal.* **2022**, *12* (15), 9735−9752.

(11) Xiao, C.; Zhang, J. Architectural design for enhanced C_2 product selectivity in electrochemical CO_2 reduction using Cu-based catalysts: A review. *ACS Nano* **2021**, *15* (5), 7975−8000.

(12) Ren, Q.; Zhang, N.; Dong, Z.; Zhang, L.; Chen, X.; Luo, L. Structural evolution of Cu_2O nanocube electrocatalysts for the CO_2 reduction reaction. *Nano Energy* **2023**, *106*, 108080.

(13) Li, J.; Xu, K.; Liu, F.; Li, Y.; Hu, Y.; Chen, X.; Wang, H.; Xu, W.; Ni, Y.; Ding, G.; Zhao, T.; Yu, M.; Xie, W.; Cheng, F. Hollow hierarchical Cu_2O-derived electrocatalysts steering CO_2 reduction to multi-carbon chemicals at low overpotentials. *Adv. Mater.* **2023**, *35* (26), No. e2301127.

(14) Chhetri, M.; Wan, M.; Jin, Z.; Yeager, J.; Sandor, C.; Rapp, C.; Wang, H.; Lee, S.; Bodenschatz, C. J.; Zachman, M. J.; Che, F.; Yang, M. Dual-site catalysts featuring platinum-group-metal atoms on copper shapes boost hydrocarbon formations in electrocatalytic CO_2 reduction. *Nat. Commun.* **2023**, *14* (1), 3075.

(15) Zhao, Y.; Liu, X.; Chen, D.; Liu, Z.; Yang, Q.; Lin, X.; Peng, M.; Liu, P.; Tan, Y. Atomic-level-designed copper atoms on hierarchically porous gold architectures for high-efficiency electrochemical CO_2 reduction. *Sci. China Mater.* **2021**, *64* (8), 1900−1909.

(16) Wang, P.; Meng, S.; Zhang, B.; He, M.; Li, P.; Yang, C.; Li, G.; Li, Z. Sub-1 nm Cu_2O nanosheets for the electrochemical CO_2 reduction and valence state−activity relationship. *J. Am. Chem. Soc.* **2023**, *145* (48), 26133−26143.

(17) Lei, L.; Huang, D.; Cheng, M.; Deng, R.; Chen, S.; Chen, Y.; Wang, W. Defects engineering of bimetallic Ni-based catalysts for electrochemical energy conversion. *Coord. Chem. Rev.* **2020**, *418*, 213372.

(18) Pan, F.; Yang, Y. Designing CO_2 reduction electrode materials by morphology and interface engineering. *Energy Environ. Sci.* **2020**, *13*, 2275−2309.

(19) Liu, F.; Fan, Z. Defect engineering of two-dimensional materials for advanced energy conversion and storage. *Chem. Soc. Rev.* **2023**, *52* (5), 1723−1772.

(20) Yang, C. D.; Gao, Y.; Ma, T.; Bai, M. R.; He, C.; Ren, X. C.; Luo, X. L.; Wu, C. Z.; Li, S.; Cheng, C. Metal alloys-structured electrocatalysts: Metal-metal interactions, coordination microenvironments, and structural property-reactivity relationships. *Adv. Mater.* **2023**, *35* (51), 2301836.

(21) He, C.; Gong, Y.; Li, S.; Wu, J.; Lu, Z.; Li, Q.; Wang, L.; Wu, S.; Zhang, J. Single-atom alloys materials for CO_2 and CH_4 catalytic conversion. *Adv. Mater.* **2024**, *36* (16), 2311628.

(22) Xie, C.; Niu, Z.; Kim, D.; Li, M.; Yang, P. Surface and interface control in nanoparticle catalysis. *Chem. Rev.* **2020**, *120* (2), 1184−1249.

(23) Xie, F.; Wang, Z.; Kao, C. W.; Lan, J.; Lu, Y. R.; Tan, Y. Asymmetric local electric field induced by dual heteroatoms on copper boosts efficient CO_2 reduction over ultrawide potential window. *Angew. Chem., Int. Ed.* **2024**, *63* (37), No. e202407661.

(24) Yu, Y.; Jiang, K.; Luo, M.; Zhao, Y.; Lan, J.; Peng, M.; de Groot, F. M. F.; Tan, Y. Self-activated catalytic sites on nanoporous dilute alloy for high-efficiency electrochemical hydrogen evolution. *ACS Nano* **2021**, *15* (3), 5333−5340.

(25) Nitopi, S.; Bertheussen, E.; Scott, S. B.; Liu, X.; Engstfeld, A. K.; Horch, S.; Seger, B.; Stephens, I. E. L.; Chan, K.; Hahn, C.; Norskov, J. K.; Jaramillo, T. F.; Chorkendorff, I. Progress and perspectives of electrochemical CO_2 reduction on copper in aqueous electrolyte. *Chem. Rev.* **2019**, *119* (12), 7610−7672.

(26) Du, C.; Mills, J. P.; Yohannes, A. G.; Wei, W.; Wang, L.; Lu, S.; Lian, J.-X.; Wang, M.; Guo, T.; Wang, X.; Zhou, H.; Sun, C.-J.; Wen, J. Z.; Kendall, B.; Couillard, M.; Guo, H.; Tan, Z.; Siahrostami, S.; Wu, Y. A. Cascade electrocatalysis via AgCu single-atom alloy and Ag nanoparticles in CO_2 electroreduction toward multicarbon products. *Nat. Commun.* **2023**, *14* (1), 6142.

(27) Wang, J.; Sun, M.; Xu, H.; Hao, F.; Wa, Q.; Su, J.; Zhou, J.; Wang, Y.; Yu, J.; Zhang, P.; Ye, R.; Chu, S.; Huang, B.; Shao, M.; Fan, Z. Coordination environment engineering of metal centers in coordination polymers for selective carbon dioxide electroreduction toward multicarbon products. *ACS Nano* **2024**, *18* (9), 7192−7203.

(28) Guo, L.; Zhou, J.; Liu, F.; Meng, X.; Ma, Y.; Hao, F.; Xiong, Y.; Fan, Z. Electronic structure design of transition metal-based catalysts for electrochemical carbon dioxide reduction. *ACS Nano* **2024**, *18* (14), 9823−9851.

(29) Shen, T.; Wang, S.; Zhao, T.; Hu, Y.; Wang, D. Recent advances of single-atom-alloy for energy electrocatalysis. *Adv. Energy Mater.* **2022**, *12* (39), 2201823.

(30) Hannagan, R. T.; Giannakakis, G.; Flytzani-Stephanopoulos, M.; Sykes, E. C. H. Single-atom alloy catalysis. *Chem. Rev.* **2020**, *120* (21), 12044−12088.

(31) Xu, Z. L.; Ao, Z. M.; Yang, M.; Wang, S. B. Recent progress in single-atom alloys: Synthesis, properties, and applications in environmental catalysis. *J. Hazard. Mater.* **2022**, *424*, 127427.

(32) Ma, Y.; Yu, J.; Sun, M.; Chen, B.; Zhou, X.; Ye, C.; Guan, Z.; Guo, W.; Wang, G.; Lu, S.; Xia, D.; Wang, Y.; He, Z.; Zheng, L.; Yun, Q.; Wang, L.; Zhou, J.; Lu, P.; Yin, J.; Zhao, Y.; Luo, Z.; Zhai, L.; Liao, L.; Zhu, Z.; Ye, R.; Chen, Y.; Lu, Y.; Xi, S.; Huang, B.; Lee, C. S.; Fan, Z. Confined Growth of Silver−Copper Janus Nanostructures with {100} Facets for Highly Selective Tandem Electrocatalytic Carbon Dioxide Reduction. *Adv. Mater.* **2022**, *34* (19), No. e2110607.

(33) Ma, Y.; Sun, M.; Xu, H.; Zhang, Q.; Lv, J.; Guo, W.; Hao, F.; Cui, W.; Wang, Y.; Yin, J.; Wen, H.; Lu, P.; Wang, G.; Zhou, J.; Yu, J.; Ye, C.; Gan, L.; Zhang, D.; Chu, S.; Gu, L.; Shao, M.; Huang, B.; Fan, Z. Site-selective growth of fcc-2H-fcc copper on unconventional phase metal

https://doi.org/10.1021/acsnano.4c13961
ACS Nano 2025, 19, 4505−4514

nanomaterials for highly efficient tandem CO_2 electroreduction. *Adv. Mater.* **2024**, *36* (32), No. e2402979.
(34) Chen, C.; Li, Y.; Yu, S.; Louisia, S.; Jin, J.; Li, M.; Ross, M. B.; Yang, P. Cu-Ag tandem catalysts for high-rate CO_2 electrolysis toward multicarbons. *Joule* **2020**, *4* (8), 1688−1699.
(35) Liu, M.; Wang, Q.; Luo, T.; Herran, M.; Cao, X.; Liao, W.; Zhu, L.; Li, H.; Stefancu, A.; Lu, Y.-R.; Chan, T.-S.; Pensa, E.; Ma, C.; Zhang, S.; Xiao, R.; Cortés, E. Potential alignment in tandem catalysts enhances CO_2-to-C_2H_4 conversion efficiencies. *J. Am. Chem. Soc.* **2024**, *146* (1), 468−475.
(36) Zhang, B.; Zhang, J.; Hua, M.; Wan, Q.; Su, Z.; Tan, X.; Liu, L.; Zhang, F.; Chen, G.; Tan, D.; Cheng, X.; Han, B.; Zheng, L.; Mo, G. Highly electrocatalytic ethylene production from CO_2 on nano-defective Cu nanosheets. *J. Am. Chem. Soc.* **2020**, *142*, 13606−13613.
(37) Wang, Q.; Lei, Y.; Wang, D.; Li, Y. Defect engineering in earth-abundant electrocatalysts for CO_2 and N_2 reduction. *Energy Environ. Sci.* **2019**, *12*, 1730−1750.
(38) Zhang, Y.; Chen, Y.; Wang, X.; Feng, Y.; Dai, Z.; Cheng, M.; Zhang, G. Low-coordinated copper facilitates the $*CH_2CO$ affinity at enhanced rectifying interface of Cu/Cu_2O for efficient CO_2-to-multicarbon alcohols conversion. *Nat. Commun.* **2024**, *15* (1), 5172.
(39) Liu, K.; Li, H.; Xie, M.; Wang, P.; Jin, Z.; Liu, Y.; Zhou, M.; Li, P.; Yu, G. Thermally enhanced relay electrocatalysis of nitrate-to-ammonia reduction over single-atom-alloy oxides. *J. Am. Chem. Soc.* **2024**, *146* (11), 7779−7790.
(40) Li, J.; Zeng, H.; Dong, X.; Ding, Y.; Hu, S.; Zhang, R.; Dai, Y.; Cui, P.; Xiao, Z.; Zhao, D.; Zhou, L.; Zheng, T.; Xiao, J.; Zeng, J.; Xia, C. Selective CO_2 electrolysis to CO using isolated antimony alloyed copper. *Nat. Commun.* **2023**, *14* (1), 340.
(41) Li, Z.; Wang, P.; Lyu, X.; Kondapalli, V. K. R.; Xiang, S.; Jimenez, J. D.; Ma, L.; Ito, T.; Zhang, T.; Raj, J.; Fang, Y.; Bai, Y.; Li, J.; Serov, A.; Shanov, V.; Frenkel, A. I.; Senanayake, S. D.; Yang, S.; Senftle, T. P.; Wu, J. Directing CO_2 electroreduction pathways for selective C_2 product formation using single-site doped copper catalysts. *Nat. Chem. Eng.* **2024**, *1* (2), 159−169.
(42) Kuhn, M.; Sham, T. K. Charge redistribution and electronic behavior in a series of Au-Cu alloys. *Phys. Rev. B* **1994**, *49* (3), 1647−1661.
(43) Jiao, J.; Kang, X.; Yang, J.; Jia, S.; Peng, Y.; Liu, S.; Chen, C.; Xing, X.; He, M.; Wu, H.; Han, B. Steering the reaction pathway of CO_2 electroreduction by tuning the coordination number of copper catalysts. *J. Am. Chem. Soc.* **2024**, *146* (23), 15917−15925.
(44) Chen, C. H.; Wu, D.; Li, Z.; Zhang, R.; Kuai, C. G.; Zhao, X. R.; Dong, C. K.; Qiao, S. Z.; Liu, H.; Du, X. W. Ruthenium-based single-atom alloy with high electrocatalytic activity for hydrogen evolution. *Adv. Energy Mater.* **2019**, *9* (20), 1803913.
(45) Gao, Q.; Yao, B.; Pillai, H. S.; Zang, W.; Han, X.; Liu, Y.; Yu, S.-W.; Yan, Z.; Min, B.; Zhang, S.; Zhou, H.; Ma, L.; Xin, H.; He, Q.; Zhu, H. Synthesis of core/shell nanocrystals with ordered intermetallic single-atom alloy layers for nitrate electroreduction to ammonia. *Nat. Synth.* **2023**, *2*, 624−634.
(46) Liu, S. B.; Lu, X. F.; Xiao, J.; Wang, X.; Lou, X. W. Bi_2O_3 nanosheets grown on multi-channel carbon matrix to catalyze efficient CO_2 electroreduction to HCOOH. *Angew. Chem., Int. Ed.* **2019**, *58* (39), 13828−13833.
(47) Gao, S.; Sun, Z.; Liu, W.; Jiao, X.; Zu, X.; Hu, Q.; Sun, Y.; Yao, T.; Zhang, W.; Wei, S.; Xie, Y. Atomic layer confined vacancies for atomic-level insights into carbon dioxide electroreduction. *Nat. Commun.* **2017**, *8* (1), 14503.
(48) Guo, W.; Zhang, S.; Zhang, J.; Wu, H.; Ma, Y.; Song, Y.; Cheng, L.; Chang, L.; Li, G.; Liu, Y.; Wei, G.; Gan, L.; Zhu, M.; Xi, S.; Wang, X.; Yakobson, B. I.; Tang, B. Z.; Ye, R. Accelerating multielectron reduction at Cu_xO nanograins interfaces with controlled local electric field. *Nat. Commun.* **2023**, *14* (1), 7383.
(49) Delmo, E. P.; Wang, Y.; Song, Y.; Zhu, S.; Zhang, H.; Xu, H.; Li, T.; Jang, J.; Kwon, Y.; Wang, Y.; Shao, M. In situ infrared spectroscopic evidence of enhanced electrochemical CO_2 reduction and C−C coupling on oxide-derived copper. *J. Am. Chem. Soc.* **2024**, *146* (3), 1935−1945.
(50) Zhu, S.; Li, T.; Cai, W.-B.; Shao, M. CO_2 electrochemical reduction as probed through infrared spectroscopy. *ACS Energy Lett.* **2019**, *4* (3), 682−689.
(51) Katayama, Y.; Nattino, F.; Giordano, L.; Hwang, J.; Rao, R. R.; Andreussi, O.; Marzari, N.; Shao-Horn, Y. An in situ surface-enhanced infrared absorption spectroscopy study of electrochemical CO_2 reduction: Selectivity dependence on surface C-bound and O-bound reaction intermediates. *J. Phys. Chem. C* **2019**, *123* (10), 5951−5963.
(52) Kim, Y.; Park, S.; Shin, S. J.; Choi, W.; Min, B. K.; Kim, H.; Kim, W.; Hwang, Y. J. Time-resolved observation of C-C coupling intermediates on Cu electrodes for selective electrochemical CO_2 reduction. *Energy Environ. Sci.* **2020**, *13* (11), 4301−4311.
(53) Xiong, W.-F.; Si, D.-H.; Li, H.-F.; Song, X.; Wang, T.; Huang, Y.-B.; Liu, T.-F.; Zhang, T.; Cao, R. Steering CO_2 electroreduction selectivity u-turn to ethylene by Cu−Si bonded interface. *J. Am. Chem. Soc.* **2024**, *146* (1), 289−297.
(54) Xiong, L.; Zhang, X.; Yuan, H.; Wang, J.; Yuan, X.; Lian, Y.; Jin, H.; Sun, H.; Deng, Z.; Wang, D.; Hu, J.; Hu, H.; Choi, J.; Li, J.; Chen, Y.; Zhong, J.; Guo, J.; Rümmerli, M. H.; Xu, L.; Peng, Y. Breaking the linear scaling relationship by compositional and structural crafting of ternary Cu−Au/Ag nanoframes for electrocatalytic ethylene production. *Angew. Chem., Int. Ed.* **2021**, *60* (5), 2508−2518.
(55) Wei, D.; Wang, Y.; Dong, C. L.; Zhang, Z.; Wang, X.; Huang, Y. C.; Shi, Y.; Zhao, X.; Wang, J.; Long, R.; Xiong, Y.; Dong, F.; Li, M.; Shen, S. Decrypting the controlled product selectivity over Ag-Cu bimetallic surface alloys for electrochemical CO_2 reduction. *Angew. Chem., Int. Ed.* **2023**, *62* (19), No. e202217369.
(56) Todorova, T. K.; Schreiber, M. W.; Fontecave, M. Mechanistic understanding of CO_2 reduction reaction (CO_2RR) toward multi-carbon products by heterogeneous copper-based catalysts. *ACS Catal.* **2020**, *10* (3), 1754−1768.
(57) Zhang, D.; Zhang, H.; Guo, L.; Zheng, K.; Han, X.; Zhang, Z. Delicate control of crystallographic facet-oriented Cu_2O nanocrystals and the correlated adsorption ability. *J. Mater. Chem. A* **2009**, *19*, 5220−5225.

https://doi.org/10.1021/acsnano.4c13961
ACS Nano 2025, 19, 4505−4514